## COMMUNICATION

# Continuous gas-phase synthesis of metal oxide–graphene hybrid nanoflakes for the enhancement of lithium storage†

Jeong Hoon Byeon[a] and Young-Woo Kim*[b]

A continuous gas-phase approach has been developed to prepare tin oxide ($SnO_x$)–reduced graphene oxide (rGO) hybrid nanoflakes *via* a single-pass process. According to the TEM analysis, the $SnO_x$ particles are only distributed on the rGO particles from the gas-phase process. The hybrid particles obtained have a theoretical capacity of 774 mA h g$^{-1}$, and after 50 cycles the charge capacity of the hybrid particles still remained at 671 mA h g$^{-1}$, that is, with 86.7% retention of the reversible capacity. The dimensional confinement of the $SnO_x$ particles by the surrounding rGO limits the volume expansion upon lithium insertion, and the pores between the $SnO_x$ and rGO could be used as buffered spaces during charge–discharge, resulting in superior cyclic performances.

Graphene oxide (GO) or graphene [*i.e.* reduced GO (rGO)] has attracted much interest for its unique physical and chemical properties and wide-ranging technological applications.[1–3] Moreover, interest in nanocomposites or hybrid nanomaterials has been ever-growing, which is ascribed to their peculiarities in combining desirable properties of building blocks for a given application.[4] Besides the applications of GO and rGO, there is a great desire to fabricate composites or hybrid materials which integrate GO or rGO with nanoparticles, polymers, or even nanotubes and fullerenes.[5]

It is of great importance to bind metal oxide nanoparticles onto GO or rGO because the combination and interaction between the nanoparticles and GO or rGO will lead to multifunctional or even completely new properties in such a nanocomposite.[6] Transition metal oxides have been studied as alternative active materials for lithium ion batteries (LIBs) because of their high specific capacity. Among them, tin oxide could be a good substitute for the carbon electrode in LIBs because its high theoretical lithium storage capacity of 782 mA h g$^{-1}$ is much larger than that of graphite (372 mA h g$^{-1}$). However, similar to other lithium reactive electrode materials, tin oxide shows a very large volume change of about

300% during the charge–discharge process, which causes crumbling and cracking of the electrode. Therefore, the fabrication of tin oxide–graphene hybrid nanomaterials has recently been proved to be an effective method to improve the cyclability due to the cushion effect of the carbon component.[6–9] Graphene layers incorporated with the nanoparticles can provide a buffer for the volume change and prevent the aggregation of the particles.[10,11] Tin oxide–graphene hybrid nanomaterials have been fabricated by mechanical mixing[8] and *in situ* chemical synthesis,[6,7,9,12–14] however, the metal oxide hybridization on graphene also requires additional chemical steps and controls for the preparation of metal oxide nanoparticles,[7] and thus it is still a challenge to prepare hybrid/functional nanomaterials under simple and continuous conditions.[10,11,15]

The present work introduces a gas-phase continuous fabrication method for tin oxide ($SnO_x$) decorated rGO hybrid nanoflakes and their application for lithium storage. A serial reactor consisting of a plasma discharge coupled to a gas-phase assembly device was used to fabricate the hybrid nanoflakes. The use of plasma discharges for nanoscale materials synthesis is a rapidly developing field. In particular, non-thermal plasmas at atmospheric pressure are attractive because of several factors conducive to efficiency.[16,17] Moreover, morphological functionalization of GO through a gas-phase process was recently employed.[18] As shown in Scheme 1, freshly spark generated graphite nanoparticles (step 1)[19] were first immersed in an ultrasound-impinging device (step 2, refer to Fig. S1, ESI†) containing a simplified Hummers' solution (step 1′)[20] to form GO (refer to Fig. S1, ESI†). The reacted solution containing the GO was injected into the reservoir of a Collison atomizer, and then atomized as droplets (step 3). The droplets were passed through a denuder (step 4), and were then immersed in the other ultrasound-impinging device to be photoreduced as rGO. The immersed GO particles as a dispersion were treated with UV (306 nm) irradiation (step 5). During this treatment, the hydrated electrons act as reducing agents to reduce GO to rGO (also refer to Scheme 1). This is because water exhibits a high absorption cross section for UV irradiation and homolyzes upon excitation into hydrogen atoms, hydroperoxyl radicals, and hydrated electrons.[3] Another spark discharge generated $SnO_x$

[a]*Department of Chemistry, Purdue University, Indiana 47907, United States*
[b]*Department of Automotive Engineering, Hoseo University, Asan 336-795, Republic of Korea. E-mail: ywkim@hoseo.edu; Fax: +82 41 540 5818; Tel: +82 41 540 5819*
† Electronic supplementary information (ESI) available. See DOI: 10.1039/c3ra40529j
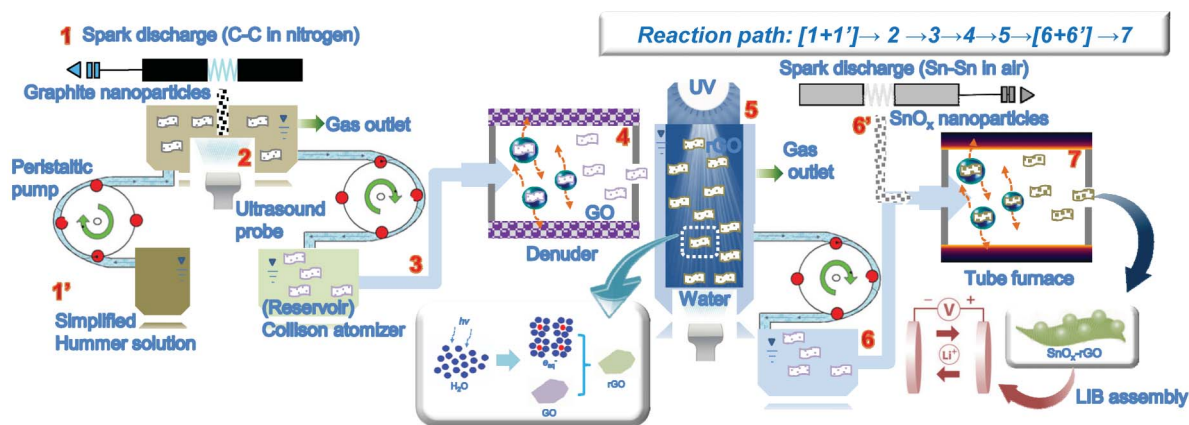
**Scheme 1** Gas-phase continuous synthesis of SnO$_x$–rGO using a serial reactor consisting of spark discharges, Collison atomizers, and ultrasound probe inserted impingers.

nanoparticles (step 6′), and the particle laden flow passed over the other Collison atomizer orifice where they mixed with the atomized rGO solution to form hybrid droplets (step 6). The droplets then passed through a heated tubular reactor to drive water from the droplets (step 7), resulting in SnO$_x$–rGO hybrid nanoparticles. The collected hybrid particles were finally employed as the active material of a LIB.

SnO$_x$–rGO hybrid particles were formed by incorporating SnO$_x$ with rGO during atomization of the rGO solution. We verified a merge between SnO$_x$ and rGO by measuring the size distributions of SnO$_x$, rGO, and SnO$_x$–rGO aerosol particles. The size distribution was measured using a scanning mobility particle sizer (SMPS, 3936, TSI, US). Fig. 1a summarizes the size distribution measurements of the SnO$_x$, rGO, and SnO$_x$–rGO particles. The total number concentration (TNC), geometric mean diameter (GMD), and geometric standard deviation (GSD) of SnO$_x$–rGO were 3.03 × 10$^6$ cm$^{-3}$, 31.8 nm, and 1.47, respectively. Analogous data for individual SnO$_x$ particles were 5.81 × 10$^6$ cm$^{-3}$, 33.8 nm, and 1.47, respectively, and for individual rGO particles were 2.35 × 10$^6$ cm$^{-3}$, 34.5 nm, and 1.52, respectively. The size distribution of

SnO$_x$–rGO was more similar to that of the rGO particles than that of the SnO$_x$ particles, and there was no bimodal distribution character, implying that the SnO$_x$ particles were nearly quantitatively incorporated with the rGO, to form SnO$_x$–rGO hybrid nanoparticles.

Low and high magnification transmission electron microscope (TEM, JEM-3010, JEOL, Japan) images show the morphology of SnO$_x$, rGO, and SnO$_x$–rGO. The TEM images (Fig. 2a) reveal that the SnO$_x$ particles were agglomerates of several primary particles (each ∼4 nm in diameter). In the inset of Fig. 2a, a lattice fringe size of about 0.33 nm was observed for SnO$_x$, which can be indexed as the (110) plane of the tetragonal structure (can also be seen in Fig. S2, ESI†). From energy dispersive X-ray (JED-2200, JEOL, Japan) analyses, the chemical formula of the SnO$_x$ particles can be defined as SnO$_{2.08}$. Fig. 2b shows the rGO particles after photoreduction in the presence of water under UV irradiation. There are no significant differences in the morphology before (GO, refer to Fig. S1, ESI†) and after the reduction, however, the mean mode diameter of GO decreased from ∼37 nm to ∼33 nm and it became brighter than before the reduction. According to a report by Stankovich et al.,[21] the new graphitic domains created during the reduction of GO to rGO are smaller in size (i.e. smaller in-plane sp$^2$ domains are formed) than the size of GO before reduction. The structural differences between GO and rGO were also verified using a Fourier transform infrared spectrometer (Nicolet 6700, Thermo Electron, US, refer to Fig. S3, ESI†). When the SnO$_x$ particles passed over the orifice of the Collison atomizer, most SnO$_x$ particles were attached on the rGO particles, resulting in SnO$_x$–rGO hybrid particles (Fig. 2c). The production yield of SnO$_x$–rGO from the gas-phase synthesis is approximately 94%. The yield was determined by the area fraction of SnO$_x$–rGO-to-all particles in the TEM image. Moreover, the SnO$_x$ particles were redistributed on the rGO particles due to deagglomeration (by setting the force acting on an agglomerate of size $D_{pa}$ due to the sudden pressure change across the orifice in the Collison atomizer), which is given by[22]
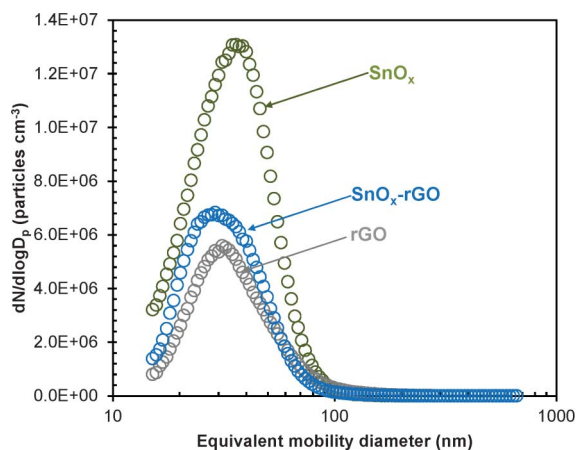
$$D_{pr} = \alpha\sqrt{\frac{D_{pa}H}{6\pi\Delta P\Theta^2}} \qquad (1)$$



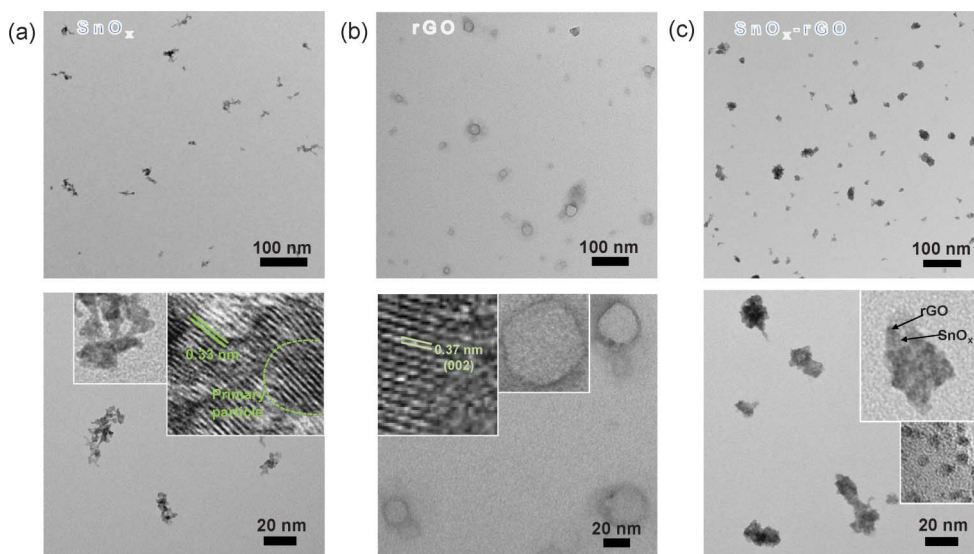**Fig. 1** Size distributions of aerosol SnO$_x$, rGO and SnO$_x$–rGO particles.

**Fig. 2** TEM images of aerosol particles of (a) $SnO_x$, (b) rGO, and (c) $SnO_x$–rGO.

where $D_{pr}$ is the size of a restructured agglomerate, $\alpha$ is the proportionality constant, $H$ is the Hamaker constant, $\Delta P$ is the pressure difference between the front and the rear of the orifice, and $\Theta$ is the parameter controlling the maximum cohesive strength between constituting particles in an agglomerate. $SnO_x$ agglomerates passed through the orifice, and the rapid changes in pressure, density, and velocity across the orifice produced an impulse capable of shattering the agglomerates. This induced a decrease in the fractal dimension of the $SnO_x$ particles on rGO, and thus the number $N$ of agglomerates after passing though the orifice was smaller than it would be for spark generated $SnO_x$ particles (see eqn (2), where $k_g$ is the fractal prefactor, $D_{p0}$ is the size of primary $SnO_x$ particles, and $d_f$ is the fractal dimension).

$$N = k_g \left(\frac{D_{pr}}{D_{p0}}\right)^{d_f} \quad (2)$$

Therefore, the actual number $N_a$ of $SnO_x$ particles to be incorporated on rGO increased by decreasing $N$ (see eqn (3), where $N_p$ is the number of primary $SnO_x$ particles), and subsequently, their surface area $S$ increased (see eqn (4), where $m_{SnOx}$ is the unit mass of the $SnO_x$ particles).

$$\frac{N_p}{N_a} = N \quad (3)$$

$$S \approx \frac{N_a \pi D_{pa}^2}{m_{SnO_x}} \quad (4)$$

It seems that the incorporation of $SnO_x$ on rGO inhibited the dislocation of $SnO_x$ from rGO during aerosol delivery. This is due to the capillary ($F_{cap} = 4\pi r_p \gamma \cos\theta$, where $r_p$, $\gamma$, and $\theta$ are the particle radius, surface tension, and contact angle, respectively, between

$SnO_x$ and rGO) and the electrostatic attraction ($F_{ea} = \dfrac{1}{4\pi\varepsilon_0}\dfrac{q_1 q_2}{d^2}$, where $\varepsilon_0$ is the permittivity constant, $d$ is the distance between $SnO_x$ and rGO, and $q_1$ and $q_2$ are the surface charges of $SnO_x$ and rGO, respectively) forces between $SnO_x$ and rGO. Spark generated particles normally have positive charges owing to a photon- and/or electron-induced ionization of their surface during spark particle formation.[23] In addition, rGO has negative charges from the remaining carboxylates on its structure.[24]

In order to examine the applicability of the fabricated hybrids to the electrochemical performance as active materials, we investigated the lithium insertion–extraction properties of the fabricated $SnO_x$–rGO hybrid nanoparticles (the mass ratio between $SnO_x$ and rGO was approximately 7.46). The electrodes were fabricated by mixing the hybrid particles with a binder, poly(vinylidene fluoride) [PVDF], and they were then tested in lithium battery coin cells at a constant current density of 50 mA $g^{-1}$. The voltage range was fixed from 0 to 2 V. Fig. 3a shows the charge–discharge profiles of a $SnO_x$–rGO electrode in the 2nd, 5th, 15th, 30th, and 50th cycles. In the first cycle (inset in Fig. 3a), the $SnO_x$–rGO electrode exhibited a lithium insertion capacity of 1 866 mA h $g^{-1}$ and a reversible capacity of 912 mA h $g^{-1}$. After 50 cycles, the charge capacity of the hybrid electrode still remained at 671 mA h $g^{-1}$. This value is higher than those from the hybridization between tin oxide and graphene in previous reports.[8,10,11,18] For further comparison, the theoretical capacity of $SnO_x$–rGO was estimated by calculating the capacity of the physical mixture of individual materials ($SnO_x$ and graphene). Based on the weight content determined by SMPS measurements and the theoretical capacity of the two components (a $C_{SnO_2}$ value of 782 mA h $g^{-1}$ and a $C_{graphene}$ value of 744 mA h $g^{-1}$), the theoretical capacity of $SnO_x$–rGO was calculated to be 774 mA h $g^{-1}$. Despite the considerable drop, the charge capacity of $SnO_x$–rGO maintained after 50 cycles still remained at 86.7% of the theoretical value, highlighting the synergetic effect for enhanced
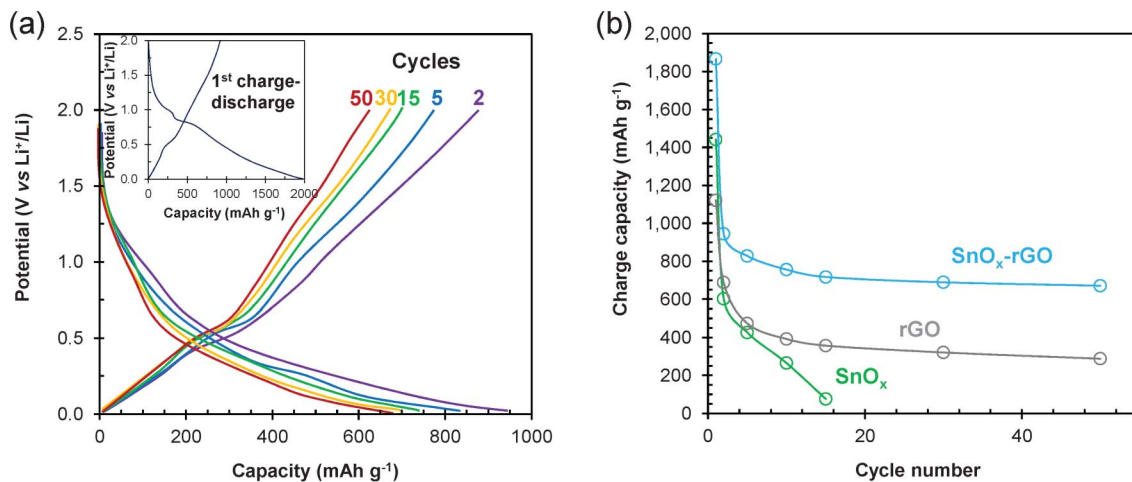
**Fig. 3** (a) Charge–discharge profiles of SnO$_x$–rGO. (b) Cyclic performances of SnO$_x$, rGO, and SnO$_x$–rGO.
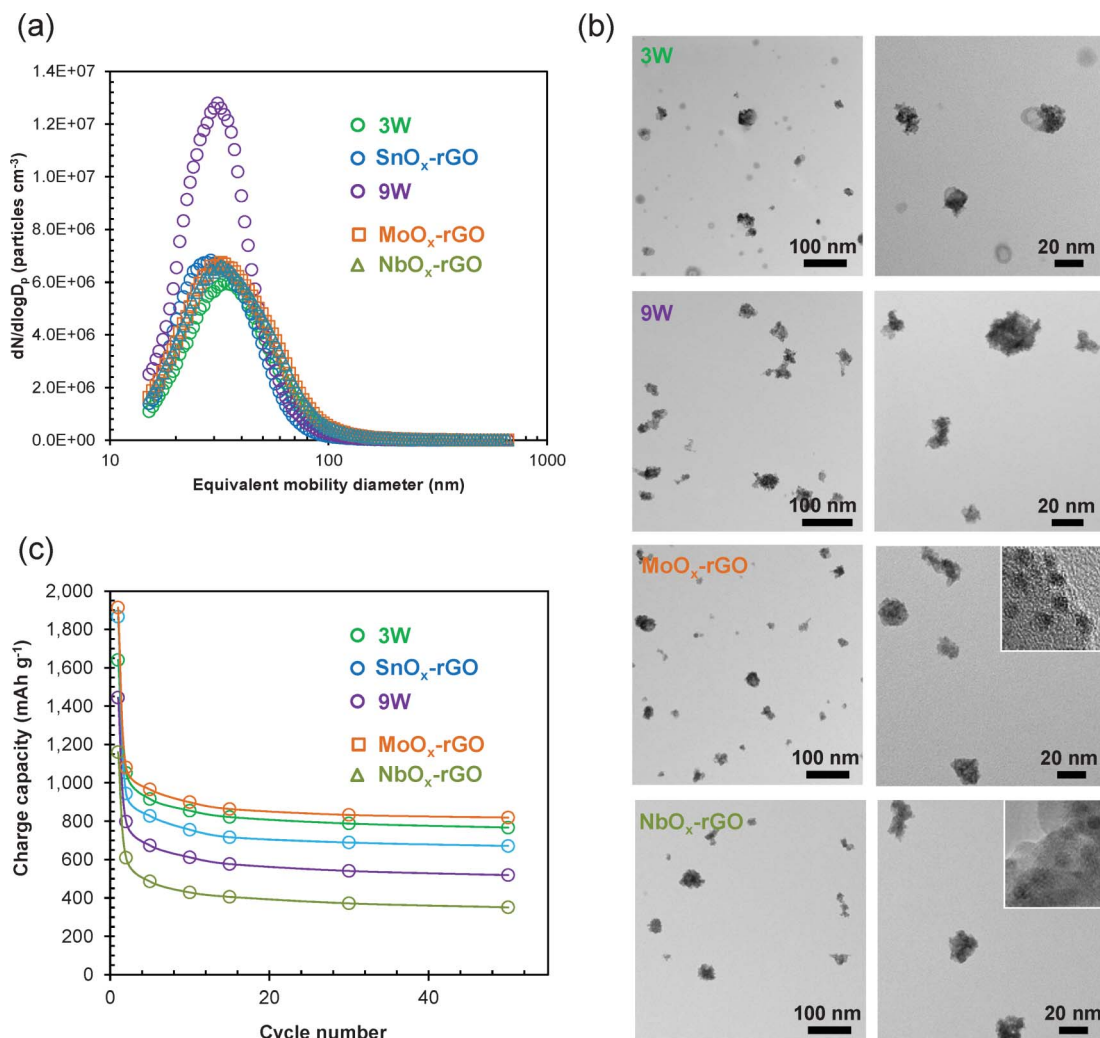


**Fig. 4** (a) Size distributions and (b) TEM images of SnO$_x$–rGO hybrid particles from different spark powers, and MoO$_x$–rGO and NbO$_x$–rGO hybrid particles from different spark configurations. (c) Cyclic performances for 3 W, 9 W, MoO$_x$–rGO, and NbO$_x$–rGO.

cyclic performance. Fig. 3b shows the cyclic performances of SnO$_x$–rGO, rGO, and SnO$_x$ particles. The individual SnO$_x$ particle electrode exhibited a poor cyclability, fading rapidly to 76 mA h g$^{-1}$ only after 15 cycles. The rGO electrode also displayed bad electrochemical performance, and showed a low reversible capacity of 288 mA h g$^{-1}$. Compared to individual SnO$_x$ particles, the reversibility of the hybrid electrode had been significantly enhanced, revealing the influence of rGO incorporations. The main reason for the poor cyclic life of individual SnO$_x$ electrodes may be due to a huge volume expansion produced by the alloying reaction between lithium and tin, leading to the pulverization and subsequent electrical disconnection of the electrodes.[4] In the case of our SnO$_x$–rGO particles, the SnO$_x$ nanoparticles are homogeneously attached to the rGO. This structural feature of the hybrid nanoparticles leads to a good connection between SnO$_x$ and rGO, which favors good electron transfer properties and effectively prevents the electrical disconnection of the electrode. The void space developed by the hybrid nanoparticles is measured to be about 0.6 cm$^3$ g$^{-1}$ based on a nitrogen adsorption measurement (refer to Fig. S4, ESI†), which offers buffer space to relieve the tension formed during the process of lithium insertion.

Fig. 4a and 4b show the size distributions and morphologies of SnO$_x$–rGO hybrid particles from different spark powers, 3 and 9 W (denoted as 3 W and 9 W vs. SnO$_x$–rGO from a 6 W spark), and also shows those of MoO$_x$– and NbO$_x$–rGO hybrid particles. These characteristics depend on their electrical and material conditions, and the details are noted in Table S1 (ESI†). According to the TEM images (Fig. 4b), the SnO$_x$ deposition density was changed when the different spark powers were applied. Moreover, the morphology of MoO$_x$– and NbO$_x$–rGO hybrid particles did not show significant differences among the hybridization cases, and this implies that the aerosol incorporation between the metal oxide and rGO was stable, although the material was changed. The reversible capacities (Fig. 4c) of 3 W and 9 W are 767 and 519 mA h g$^{-1}$, respectively. After 50 cycles, as shown in Fig. 3, the capacity of SnO$_x$–rGO remained at 671 mA h g$^{-1}$, which indicates about an 87% retention of the reversible capacity, and the 3 W and 9 W results exhibited about 81% and 64% retention of the reversible capacity, respectively. It is well known that the main reason for the rapid fading of individual tin oxide electrodes is that a large volume expansion of tin oxide occurs during the charge–discharge cycle, leading to the pulverization of the electrode. On this account, a larger ratio between SnO$_x$ and rGO from a higher power of the spark could show a faster fading character than those from smaller powers. In addition, the application of different spark configurations [molybdenum (Mo)–Mo or niobium (Nb)–Nb] can also induce different cyclic performances, and this may have originated from different theoretical charge capacities of their oxide structures.[25,26] In other words, the difference among these samples demonstrated that the cycle performance was related to the different morphology and composition of the samples. This implies that the lithium storage performance can be tuned or enhanced by controlling the ratio of the metal oxide to rGO and applying different materials of spark electrodes during the fabrication.

## Conclusions

A continuous gas-phase synthesis was developed to fabricate SnO$_x$–rGO hybrid nanoflakes in a simple and green process. The prepared hybrid particles were employed as the active material of a LIB to verify their potential application in the energy technology field. When considering the plentiful properties for both metal oxides and rGO, the hybrid nanoflakes might have other potential applications in biosensors, gas sensors, and in electrochemical analysis in the future. Furthermore, the proposed strategy described in this work opens up a new way to obtain metal oxide–rGO hybrid nanoflakes with an on-demand configuration.

## Notes and references

1  T. Wu, S. Liu, Y. Luo, W. Lu, L. Wang and X. Sun, *Nanoscale*, 2011, **3**, 2142.

2  Y. Pan, H. Bao and L. Li, *ACS Appl. Mater. Interfaces*, 2011, **3**, 4819.

3  Y. H. Ding, P. Zhang, Q. Zhuo, H. M. Ren, Z. M. Yang and Y. Jiang, *Nanotechnology*, 2011, **22**, 215601.

4  X. Huang, X. Zhou, L. Zhou, K. Qian, Y. Wang, Z. Liu and C. Yu, *ChemPhysChem*, 2011, **12**, 278.

5  X. Zhou, X. Huang, X. Qi, S. Wu, C. Xue, F. Y. C. Boey, Q. Yan, P. Chen and H. Zhang, *J. Phys. Chem. C*, 2009, **113**, 10842.

6  J. Yao, X. Shen, B. Wang, H. Liu and G. Wang, *Electrochem. Commun.*, 2009, **11**, 1849.

7  Y. Li, X. Lv, J. Lu and J. Li, *J. Phys. Chem. C*, 2010, **114**, 21770.

8  S.-M. Paek, E. Yoo and I. Honma, *Nano Lett.*, 2009, **9**, 72.

9  P. Lian, X. Zhu, S. Liang, Z. Li, W. Yang and H. Wang, *Electrochim. Acta*, 2011, **56**, 4532.

10  Z. Wen, S. Cui, H. Kim, S. Mao, K. Yu, G. Lu, H. Pu, O. Mao and J. Chen, *J. Mater. Chem.*, 2012, **22**, 3300.

11  S. Liang, X. Zhu, P. Lian, W. Yang and H. Wang, *J. Solid State Chem.*, 2011, **184**, 1400.

12  X. Wang, X. Zhou, K. Yao, J. Zhang and Z. Liu, *Carbon*, 2011, **49**, 133.

13  Z. Du, X. Yin, M. Zhang, Q. Hao, Y. Wang and T. Wang, *Mater. Lett.*, 2010, **64**, 2076.

14  L.-S. Zhang, L.-Y. Jiang, H.-J. Yan, W. D. Wang, W. Wang, W.-G. Song, Y.-G. Guo and L.-J. Wan, *J. Mater. Chem.*, 2010, **20**, 5462.

15  M. Heurlin, M. H. Magnusson, D. Lindgren, M. Ek, L. R. Wallenberg, K. Deppert and L. Samuelson, *Nature*, 2012, **492**, 90.

16  D. Z. Pai, K. Ostrikov, S. Kumar, D. A. Lacoste, I. Levchenko and C. O. Laux, *Sci. Rep.*, 2013, **3**, 1221.

17  Z. Han, B. Tay, C. Tan, M. Shakerzadeh and K. Ostrikov, *ACS Nano*, 2009, **3**, 3031.

18  S. Mao, Z. Wen, H. Kim, G. Lu, P. Hurley and J. Chen, *ACS Nano*, 2012, **6**, 7505.

19  J. H. Byeon, J. H. Park, K. Y. Yoon, B. J. Ko, J. H. Ji and J. Hwang, *Carbon*, 2006, **44**, 2106.

20  H. N. Lim, N. M. Huang and C. H. Loo, *J. Non-Cryst. Solids*, 2012, **358**, 525.

21  S. Stankovich, D. A. Kikin, R. D. Piner, K. A. Kohlhaas, A. Kleinhammes, Y. Jia, Y. Wu, S. T. Nguyen and R. S. Ruoff, *Carbon*, 2007, **45**, 1558.

22  J. H. Byeon and J. T. Roberts, *ACS Appl. Mater. Interfaces*, 2012, **4**, 2693.

23 J. H. Byeon and J.-W. Kim, *Langmuir*, 2010, **26**, 11928.

24 L. Guardia, S. Villar-Rodil, J. I. Paredes, R. Rozada, A. Martínez-Alonso and J. M. D. Tascón, *Carbon*, 2012, **50**, 1014.

25 Y. Sun, X. Hu, W. Luo and Y. Huang, *ACS Nano*, 2011, **5**, 7100.

26 M. Sasidharan, N. Gunawardhana, M. Yoshio and K. Nakashima, *Mater. Res. Bull.*, 2012, **47**, 2161.

This journal is © The Royal Society of Chemistry 2013